ACS Catalysis

Research Article

pubs.acs.org/acscatalysis

Highly Active Graphene-Supported Ni_xPd_{100-x} Binary Alloyed Catalysts for Electro-Oxidation of Ethanol in an Alkaline Media

Mohammad Shamsuddin Ahmed and Seungwon Jeon*

Department of Chemistry and Institute of Basic Science, Chonnam National University, 300 Yongbong-dong, Buk-gu, Gwangju 500-757, Republic of Korea

Supporting Information

ABSTRACT: A series of graphene (G)-supported Ni_xPd_{100-x} binary alloyed catalysts (BACs) were prepared with variation of Ni and Pd metal loading through a facile chemical reduction method and were used as an anode catalyst for ethanol oxidation reaction (EOR), which is superior fuels for direct ethanol fuel cells (DEFCs). The X-ray diffraction (XRD) data reveals that the Ni_xPd_{100-x}/G catalysts were homogeneously alloyed, and Ni was present with the oxidized form. The transmission electron microscopy (TEM) images also suggest the alloyed formation with different shapes of metal nanoparticles (NPs). The electrochemical properties of the catalysts were evaluated using cyclic voltammetry (CV) and chronoamperometry (CA) in 1 M KOH electrolyte. The higher catalytic activity for EOR was increased in the order $Ni_{75}Pd_{25}$/G > Ni_0Pd_{100}/G > $Ni_{25}Pd_{75}$/G > $Ni_{50}Pd_{50}$/G. Among Ni_xPd_{100-x}/G BACs, the $Ni_{50}Pd_{50}$/G catalyst showed the highest onset potential (−0.8 V) on CV and long-term stability on amperometric measurements. The overall parameters of EOR study were determined that the $Ni_{50}Pd_{50}$/G was more favorable in various ethanol (EtOH) concentrations and scan rate.

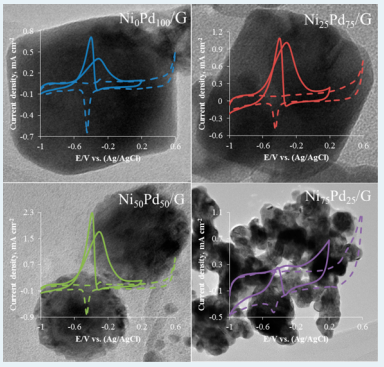

KEYWORDS: *Ni−Pd, binary alloyed catalysts, ethanol oxidation reaction, electrocatalyst, direct ethanol fuel cell*

INTRODUCTION

Platinum-containing catalysts have been used as the best electroactive catalysts for both anode and cathode in fuel cells (FCs).[1] However, they still suffer from multiple problems such as slow reaction kinetics, CO poisoning, high cost, limited reserve in nature, and poor durability.[2−7] For reducing the usage of the precious Pt metal and hereafter the cost of FCs, the progress of non-Pt electrocatalysts has thus generated a huge interest.[8,9] Alternatively, palladium is an auspicious catalyst because it is cheaper than Pt and has higher catalytic activity for small alcoholic molecules (i.e., ethanol, EtOH) oxidation for DEFCs in basic media,[8,10−14] which are considered as potential future power sources.[15,16] It is well-known that adsorbed hydroxide species could promote dehydrogenation of adsorbed alcohol and desorption of poisoning residues and thus enhance the oxidation of alcohol on Pd catalysts in alkaline medium.[17] Binary alloyed catalysts (BACs), which have been proved to be an effective way to further improve the electrocatalytic activity and tolerance to poisoning intermediates of Pd-based electrocatalysts.[18] However, the addition of a transition metal element, such as nickel to Pd can significantly improve the overall catalytic activities of Pd due to the bimetallic promotional effect.[19] In addition, the surface morphologies and sizes of electrocatalysts are playing a vital role in their catalytic activities.[20] Moreover, when two metals are alloyed, the d-band shift and the changes of segregation energy of added metals should also be responsible for bimetallic high activity of Pd catalysts, based on density functional theory.[21,22] Recently, the synthesis of Pd with Ni has attracted widespread attention due to their low cost, stability, and excellent catalytic activities.[8,15,19,20,22,23]

Various carbon materials, which are used as supports for Pd metal-based catalysts, such as carbon blacks, carbon nanotubes, carbon nitride, and carbon nanofibers[2,22−26] have been studied intensively as well in order to improve the catalytic performance. Also, two-dimensional thin material, graphene (G)-supported Pd catalysts,[10,27] including alloy[11,28] and core−shell[29] have been investigated. It is well-known that G has attracted much attention in the last several years owing to its unique properties,[30,31] including thermal and electrical conductivity, incredible strength, higher explicit surface area, and cost effectiveness.[32−35] It is expected that the addition of G can not only maximize the specific surface area of nanosized electrocatalyst for electron transfer but also provide enhanced mass transport of reactants to the electrocatalyst. However, very few G-supported Pd[10,27] and Pd-based alloys[11,28] have been reported for the ethanol oxidation reaction (EOR), including the core−shell from Zhang et al.[29] So far, for the first time we are applying on G-supported Ni_xPd_{100-x} (hereafter, denoted as Ni_xPd_{100-x}/G) BACs for EOR.

On the basis of the above considerations, we synthesized Ni_xPd_{100-x}/G BACs via simple chemical process, which has the following merits: First, the Ni is easily alloyed with Pd to form BAC in low temperature, because it is hard to alloy Ni and Pd

Received: January 23, 2014
Revised: March 31, 2014
Published: April 30, 2014

   dx.doi.org/10.1021/cs500103a | ACS Catal. 2014, 4, 1830−1837

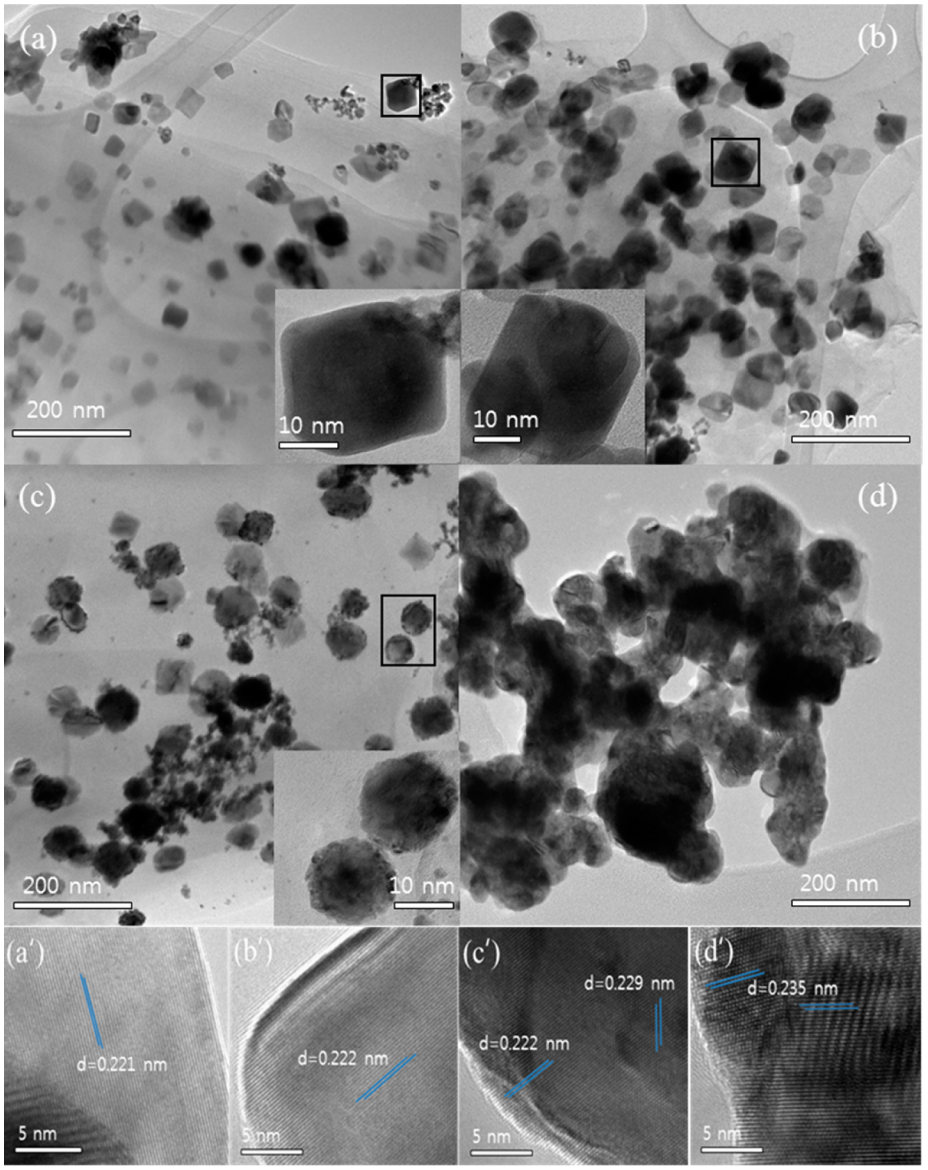

Figure 1. TEM images of Ni_0Pd_{100}/G (a), $Ni_{25}Pd_{75}$/G (b), $Ni_{50}Pd_{50}$/G (c), and $Ni_{75}Pd_{25}$/G (d) BACs. Insets: close-up view of selective particles and the HRTEM of respective BACs (a′−d′).

using low reduction temperature.[22] Second, the various Ni_xPd_{100-x}/G BACs are easily synthesized, and Ni can be found as an amorphous oxide form. Third, the as-prepared Ni_xPd_{100-x}/G BACs exhibited higher electrocatalysis toward EOR than that of Pd/G and Pt/C. Particularly, the results prove that the $Ni_{50}Pd_{50}$/G exhibit outstanding electrocatalysis for EOR. This study will be of great interest, and we expect our work to pioneer the development of cost-effective G-supported Pd-based alloy catalysts.

RESULTS AND DISCUSSION

Characterization of Various Ni_xPd_{100-x}/G. The transmission electron microscopy (TEM) images of as-prepared Ni_xPd_{100-x}/G BACs are shown in Figure 1, and the Pd nanocrystals were obtained with varying Ni concentrations. As shown in Figure1a, the Ni_0Pd_{100}/G consists of a clear crystal with variable size and shape on G, whereas the cubic shapes are leading with a fairly sharp angle. The cubic Pd crystal formation can be observed previous probably due to the addition of ascorbic acid.[37] Figure1b shows that the cubic Pd nanocrystals in $Ni_{25}Pd_{75}$/G exist with spherical-like structures upon addition of Ni , and the cubic crystals have relatively blunt angles. Figure1c shows a different morphology in $Ni_{50}Pd_{50}$/G. Almost all NPs are in spherical structures, although some cubic Pd nanocrystals are still visible. Finally, in Figure1d, an aggregated spherical structure can be observed due to excess Ni loading in $Ni_{75}Pd_{25}$/G. The magnified TEM images in all insets are subjected to the close observation of size and shape. The average size of the NPs were 35, 39, and 15 nm for Ni_0Pd_{100}/G, $Ni_{25}Pd_{75}$/G, and $Ni_{50}Pd_{50}$/G, respectively. High-resolution TEM (HRTEM) images are indicating that the prepared Ni_xPd_{100-x}/G BACs are entirely crystalline (Figure 1a′−d′). The lattice line spacing of NPs are 0.222, 0.234, and 0.229 nm, which represented Pd(111), (101), and (111) planes of NiO/$Ni(OH)_2$. The similar shape variations of Pd nanocrystals were observed previously upon various amount of KI addition as additive.[38] The probable shape formation mechanism of Ni_xPd_{100-x}/G BACs was dependent on the ratio of AA and

dx.doi.org/10.1021/cs500103a | ACS Catal. 2014, 4, 1830−1837

Pd precursor upon Ni precursor addition. It is, however, more or less similar to the reference.[38] The Ni−Pd binary alloyed formation was observed by the elemental mapping analysis (Figure S1). The energy-dispersive X-ray spectroscopy (EDS) pattern can be observed for the numerical analysis of elements in all Ni_xPd_{100-x}/G BACs (Figure S2).

The X-ray diffraction (XRD) patterns of all Ni_xPd_{100-x}/G BACs are shown in Figure 2, which characterizes their crystal

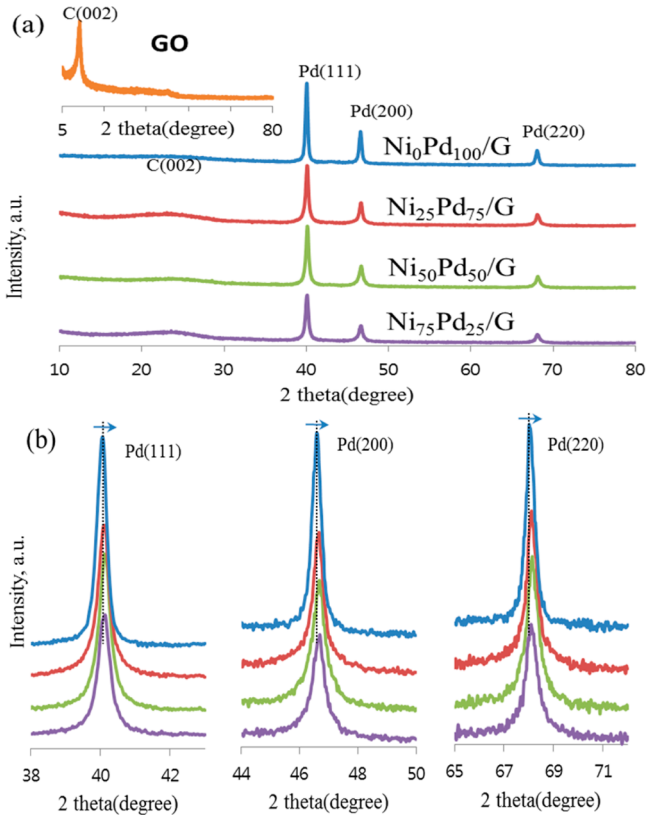

Figure 2. (a) XRD patterns of graphene supported Ni_xPd_{100-x} BACs. Inset: XRD pattern of GO. (b) Enlarged pattern of Pd(111), Pd(200), and Pd(220) peaks.

structure. In each pattern of Figure 2a, there are three characteristic typical peaks. The peaks at 2θ = 40.05°, 46.58°, and 68.06° are allocated to the Pd (111), (200), and (220), respectively. The peak at 10.8° is raised from the graphite (002) plane of GO (inset) that shifted to the higher angle at around 24.7° upon reduction. It is, however, those Pd peaks mentioned above that slightly shift to higher angles in the patterns of Ni_xPd_{100-x}/G BACs compared with those in the pattern of Ni_0Pd_{100}/G (Figure 2b). This shift indicates that Ni atoms around Pd sites had entered into the Pd lattice, forming a bimetallic transition zone.[22,39] The numeric values are listed in Table S1. No diffraction peak of Ni is observed for all BACs, indicating the Ni in BACs was amorphous in nature, although Ni can be easily oxidized in air.

The average crystallite size of the catalysts was calculated from Pd (220) peak using Scherrer eq 1[23]

$$d(\text{Å}) = \frac{k\lambda}{\beta \cos\theta} \quad (1)$$

where k is a coefficient (0.9), β the full-width at half-maximum (fwhm), λ the wavelength of X-ray used (1.5406 Å), and θ is the angle of peak maximum. The calculated crystallite sizes were 33, 35, 17, and 18 nm for Ni_0Pd_{100}/G, $Ni_{25}Pd_{75}$/G, $Ni_{50}Pd_{50}$/G, and $Ni_{75}Pd_{25}$/G BACs, respectively, which are similar to the HRTEM analysis. Also, on the basis of the same peak value, the alloying percentages for all Ni_xPd_{100-x} BACs were calculated from Vegard's law[8] and are presented in Table 1.

The X-ray photoelectron spectroscopic (XPS) spectra of GO and all Ni_xPd_{100-x}/G BACs are shown in Figure 3. The XPS recorded signals from C, O, Pd, and N for all Ni_xPd_{100-x}/G BACs, with that attributable to Pd being the most significant. However, tiny Ni 2p peaks were observed upon Ni addition, as can be seen in Figure 3a. The atomic ratio of C/O significantly increased (from 1.6 to 4.1 for GO and Ni_0Pd_{100}/G, respectively) upon the addition of reduction (Figure S3). The core level of C 1s XPS spectra of GO and all Ni_xPd_{100-x}/G BACs are shown in Figure 3b. The peak at ∼284.9 eV is attributable to the graphitic sp^2 bonds. The peaks located at 287.6 and 289.2 eV are due to the oxygenated functional groups such as C═O and O−C═O, respectively.[3,10,40] The intensity of each class of carbon can be seen in Figure S4. The spectra of all Ni_xPd_{100-x}/G BACs show a significant reduction of oxygenated functional groups compared to the GO, which is also confirmed by FTIR (Figure S5). For instance, in FTIR, the C═O (1730 cm^{-1}) peak of GO was slightly shifted to ∼1747 cm^{-1} for Ni_xPd_{100-x} all BACs, with a small appearance upon reduction. Indicating O species were reduced, and residual O atoms of G interacted with Ni_xPd_{100-x} particles by chemisorption on the surfaces of the G (C−O/Ni_xPd_{100-x}).[4] The Pd 3d spectra of all Ni_xPd_{100-x}/G BACs (Figure 3c) show two peaks at 355.6 and 340.8 eV for the $3d_{5/2}$ and $3d_{3/2}$, respectively, whereas those peaks are located at 355.3 and 340.5 eV for Ni_0Pd_{100}/G (Figure3c). Such positively shifted values indicates that the Pd in Ni_xPd_{100-x}/G BAC was present in a different electronic environment due to the alloy formation.[24,41] If we consider the more magnified spectra of

Table 1. Physical Characterization and Electrochemical Performance Comparison between of All Ni_xPd_{100-x}/G BACs

	Ni_0Pd_{100}/G	$Ni_{25}Pd_{75}$/G	$Ni_{50}Pd_{50}$/G	$Ni_{75}Pd_{25}$/G
Pd wt % from XPS analysis	50.64	46.51	39.34	24.85
Pd loading ($\mu g\ cm^{-2}$)	35.82	32.89	27.82	17.58
alloy formation (%)		48.6	73.4	36.3
ECSA ($m^2 g_{Pd}^{-1}$)	68	61	77	46
EOR onset (V vs Ag/AgCl)	−0.74	−0.77	−0.8	−0.59
j_f/j_b	0.57	0.93	0.82	1.13
mass activity (j_f, mA mg_{Pd}^{-1})	113.7	307.8	614.6	155.7
stability at 10 k s (%)	9.4	8.0	21.7	6.2
Tafel slope (mV dec^{-1})	165	160	142	591

dx.doi.org/10.1021/cs500103a | ACS Catal. 2014, 4, 1830−1837

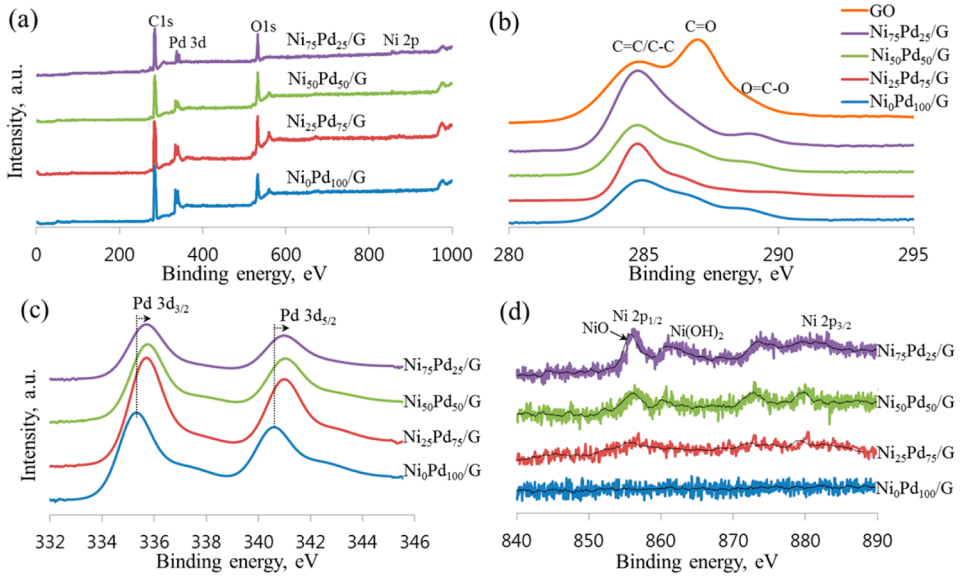

Figure 3. (a) XPS spectra, (b) core level spectra of C 1s region, (c) Pd 3d region, and (d) Ni 2p region (with trendline) for Ni_xPd_{100-x}/G BACs.

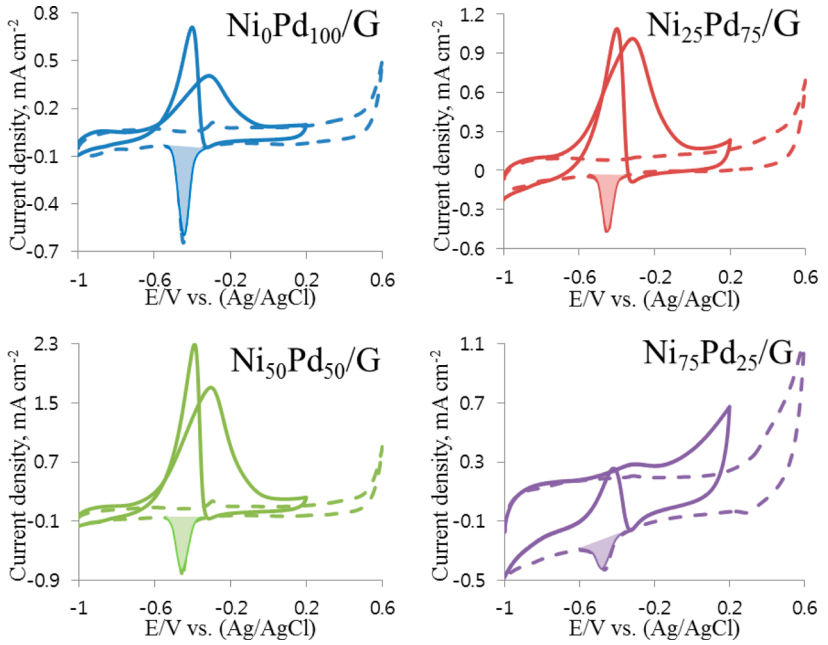

Figure 4. CVs of graphene supported Ni_xPd_{100-x} BACs recorded in 1 M KOH electrolyte in the absence (dotted lines) and presence (solid lines) of 0.1 M EtOH at a scan rate of 50 mV s^{-1}.

Pd $3d_{3/2}$, the maximum positive shifts cab be seen at $Ni_{50}Pd_{50}$/G (Figure S6), probably due to the higher degree of binary alloyed formation. Figure 3d shows the core level spectra of Ni 2p peaks, which shows a strong peak at ~855 eV, which is an indication that the Ni was in an oxide form. Also, another three salient peaks can be observed at 862, 874, and 880 eV that are attributed to the several oxo-Ni species (i.e., $Ni(OH)_2$, and NiOOH). This is probably the reason to increase the oxygen at % and decrease the C/O ratio in all BACs. The intensity of all peaks were reflected to the at% of all elements. The numeric results of all BACs have been listed in Table S2.

Electrochemical Ethanol Oxidation. The CVs of the Ni_0Pd_{100}/G, $Ni_{25}Pd_{75}$/G, $Ni_{50}Pd_{50}$/G, and $Ni_{75}Pd_{25}$/G BACs first investigated in Ar pursed 1 M KOH solution in the absence (dotted lines) and presence (solid lines) of 0.1 M ethanol are displayed in Figure 4. The dominating reduction peak of PdO at around −0.45 V in the reverse scan can be seen in all CV curves of all Ni_xPd_{100-x}/G BACs in Figure 4, and similar CVs were also observed in previous report.[8,27] The electrochemical surface area (ECSA) for all catalysts were calculated using Coulombic charge (Q) for the reduction of PdO, which is located at −0.45 V potential region (colored peaks in Figure 4).[11,8,27] The values of the ECSAs are summarized in Table 1. The highest value was obtained for $Ni_{50}Pd_{50}$/G among all catalysts and which is 1.13 times higher compared to Ni_0Pd_{100}/G. It is known that the ECSA could reveal to what degree of Pd is utilized, this result implies a better utilization of the comparatively small amount of Pd on the surface of the $Ni_{50}Pd_{50}$/G BAC with the assistance of Ni alloy formation.

dx.doi.org/10.1021/cs500103a | ACS Catal. 2014, 4, 1830−1837

The EOR on the Ni_0Pd_{100}/G, $Ni_{25}Pd_{75}$/G, $Ni_{50}Pd_{50}$/G, and $Ni_{75}Pd_{25}$/G BACs in alkaline medium was performed by CVs (Figure 4). The CV curves are similar in appearance: two well-defined peaks are observed in each curve. All two peaks are located at ∼ −0.3 V (f) in the forward sweep and located at ∼−0.4 V (b) in the backward sweep, strongly suggesting that EOR can occur on all Ni_xPd_{100-x}/G BACs in a alkaline medium, which is similar to other reports.[22,24,43] The magnitude of the forward scan peak is due to the oxidation of freshly chemisorbed species that come from the adsorption of EtOH; however, the backward scan peak is mostly associated with the removal of carbonaceous species that not completely oxidized during forward scan.[42] However, among four CVs for EOR, the current density was increased with the increasing of Ni adding up to 50 at%, and the highest current density was found with $Ni_{50}Pd_{50}$/G BAC, which is approximately 8, 4, and 1.7 times superior than that of $Ni_{75}Pd_{25}$, Ni_0Pd_{100}/G, and $Ni_{25}Pd_{75}$/G BACs, respectively. Very importantly, negatively shifted onset potential (−0.8 V) was observed on $Ni_{50}Pd_{50}$/G BAC at room temperature (RT), which is also better than that of other previous reports.[8,10,15,19,20,22−24,43]

The EOR mechanism on Pd[19,28] suggests that the carbonaceous intermediates including $(CH_3CO)_{ads}$ can be strongly adsorbed on the Pd surface and can block the activity (in the forward scan). The rate-determining step will take place in the reaction-starting region (∼−0.8 to −0.7 V), where Pd begins to adsorb OH^-. Due to the OH^- adsorption, the strongly adsorbed carbonaceous species swiftly exposed away and led to the increase in current density (peak f). It is, however, at a higher potential in the scan, and the PdO formation may block the further adsorption of reactive species and lead to a decrease in current density.[44] In the backward sweep, the earlier formed PdO would be reduced to active Pd, thus, leading to the regaining of EOR current. The newly produced Pd surface should be directly exposed to fresh ethanol. At high potential, the quick adsorption of OH^- will help with the generation of high current density and lead to a sharp backward peak. The peak b will assign to the elimination of carbonaceous species that are not completely oxidized in the forward scan,[44] and rationally, those intermediates may diffuse into the bulk solution.

It is, however, when Ni is involved that the formed $Ni(OH)_2$ of Ni_xPd_{100-x} BACs will enhance the EOR by increasing OH species that lead to the increase of onset potential and current density, as observed in Figure 5 (the forward scan's current is regularized to the mass of the Pd metal in Figure S7). In the positive and negative scans, the hydrogen adsorption/desorption region (−1.0 V to −0.8 V) was significantly depressed because of the surface blocking by EtOH decomposition. However, as the Ni amount increases, the current density at both peak f and b increases accordingly on Ni_0Pd_{100}/G > $Ni_{25}Pd_{75}$/G> $Ni_{50}Pd_{50}$/G and suddenly decrease on $Ni_{75}Pd_{25}$/G (inset). This behavior may occur for a couple of probable reasons. First, the formation of $Ni(OH)_2$ during the test increases OH^- and/or $(OH)_{ads}$ concentration into the system and facilitates to the EOR, as depicted in eq 2[19,22]

$$Pd - (CH_3CO)_{ads} + OH^- \xrightarrow{Ni(OH)_2} Pd - CH_3COOH + e^- \quad (2)$$

Second, excess Ni may block the Pd sites at $Ni_{75}Pd_{25}$/G (as observed in TEM image), leading to poor EOR due to the active surface blocking. Third, there is excellent alloy formation at $Ni_{25}Pd_{75}$/G and $Ni_{50}Pd_{50}$/G and less alloy formation than amorphous Ni at $Ni_{75}Pd_{25}$/G. The ratio of the forward peak current density (j_f) and the backward peak current density (j_b), j_f/j_b, is generally used to determine the poisoning tolerance to the carbonaceous species for Pd catalysts.[11,45] Also, a higher ratio of j_f/j_b is attributed to more efficient oxidation of EtOH and less accumulation of carbonaceous species to the catalysts. The onset potential, current density (j_f), and j_f/j_b ratio were determined by CV and are summarized in Table 1. The j_f/j_b of all BACs was higher than that of Ni_0Pd_{100}/G, which indicates that the Pd surface was less poisoned on the BACs than Ni_0Pd_{100}/G (inset).

The similar CV patterns indicate that the same EOR pathway had occurred on BACs. The EOR goes through a dual-pathway mechanism in alkaline media.[46] In the C_1 pathway, the strongly adsorbed CO_{ads} and $CH_{x,ads}$ species can be generated by C−C bond breaking. In the C_2 pathway, acetaldehyde and acetate (partially oxidized) are produced as a result of the difficulty in breaking the C−C bond. A previous report[47] showed that the carbonate formation toward EOR in alkaline media on Pd electrode was only 2.5%. Therefore, the EOR at Ni_xPd_{100-x}/G probably proceed through the C_2 pathway.[47]

The Tafel plots measured for kinetic analysis are shown in Figure 5 (see also Figure S8). Tafel slopes derived from the

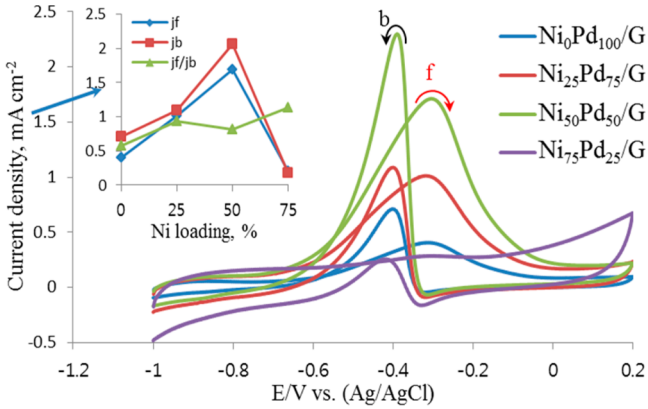

Figure 5. CVs of graphene supported Ni_xPd_{100-x} BACs were recorded in 0.1 M EtOH containing 1 M KOH electrolyte at 50 mV s^{-1} scan rate. Inset: peak potentials and j_f/j_b variation with respect to Ni loading.

linear region (from −0.7 to −0.4 V) are listed in Table 1. The slope values are 160 and 142 mV dec^{-1} for $Ni_{25}Pd_{75}$/G and $Ni_{50}Pd_{50}$/G BACs, respectively, which are lower than that of Ni_0Pd_{100}/G (165 mV dec^{-1}). Upon lower Tafel slopes, the EOR charge-transfer kinetics on the catalysts were faster than Ni_0Pd_{100}/G. The lowest Tafel slope[14,22] was found on $Ni_{50}Pd_{50}$/G that contained the highest degree of Ni and Pd alloy. Because the Ni has a strong interaction with electrolyte to form oxygenated species, it helps the EOR process through oxidation of intermediates and results in faster charge-transfer kinetics. The highest Tafel slope was found (591 mV dec^{-1}) on $Ni_{75}Pd_{25}$/G, indicating slow kinetics due to Pd surface blocking by excess Ni.

Figure 6 illustrates the potentiodynamic measurements of EOR at $Ni_{50}Pd_{50}$/G catalyst in Ar saturated 1 M KOH solutions with various EtOH concentrations. As shown in Figure 6, with increasing EtOH concentrations, the EOR starts at −0.8 V and gives rise to a peak with the same onset potential. The current density is much better than that of other reports.[14,48] There are

dx.doi.org/10.1021/cs500103a | ACS Catal. 2014, 4, 1830−1837

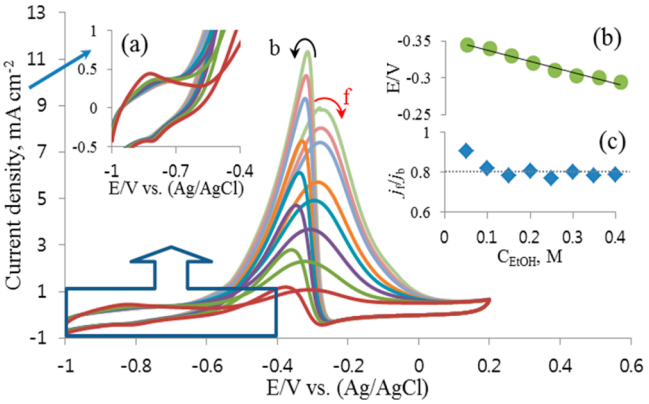

Figure 6. (a) CVs of $Ni_{50}Pd_{50}$/G recorded in 1 M KOH electrolyte with the addition of various concentrations of EtOH at 50 mV s^{-1} scan rate. Inset: enlarged CVs at −1.0 to −0.4 V. (b) Peak potential and (c) j_f/j_b vs concentrations of EtOH plots.

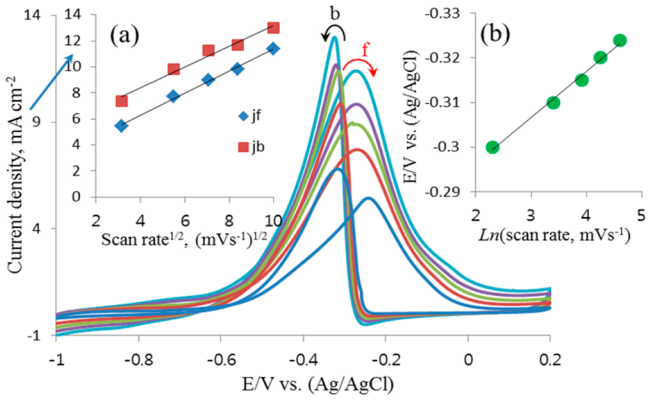

Figure 7. CVs on $Ni_{50}Pd_{50}$/G catalyst in 1 M KOH at various scan rates. Insets: plots of current density vs $v^{1/2}$ (a) and f-peak shift vs ln of scan rates (b).

some significant observations involved in the experiment: First, the onset potential of EOR on the $Ni_{50}Pd_{50}$/G is fixed (inset a). The concentration independence of the onset potential for EOR on the $Ni_{50}Pd_{50}$/G indicates that both EtOH dissociation and the oxidation of intermediate behavior at $Ni_{50}Pd_{50}$/G are the same. Also, low poisoning species may be formed at $Ni_{50}Pd_{50}$/G. Second, the CV of $Ni_{50}Pd_{50}$/G shows a couple of peaks at −0.85 and −0.38 V in the forward sweep for low concentration of EtOH (0.05 M) (inset a). The first peak is from the partial reaction current for carbonate formation (in alkaline condition), and the next peak appears due to the acetate formation (in alkaline condition).[49] For higher concentration, however, only one peak is observed in the forward scan. Third, at the −1.0 to −0.4 V potential regions, the lesser hysteresis was observed at the $Ni_{50}Pd_{50}$/G among the forward and backward sweep for EOR. Although the hysteresis is often caused by the strongly adsorbed species poisoning on the surface of electrodes,[50] $Ni_{50}Pd_{50}$/G may involve less poisoning as well as stable intermediate formation or the oxidation of these species may be fast. Fourth, small variation of peak potential ratio can be observed (inset b) with the increasing of ethanol concentration, indicating a small uncompensated resistance (IR_u) in the test system.[47] Fifth, the j_f/j_b is almost constant at around 0.8 but in the 0.05 M ethanol (inset c). The nearly constant j_f/j_b is also indicating that the stable intermediates are formed at the Pd site. The j_f/j_b for 0.05 M ethanol is higher than others, which is probably due to minimal carbonate formation earlier, as mentioned above. Also, the reproducibility has been checked in an 0.5 M EtOH-containing 1 M KOH solution (Figure S9).

Figure 7 demonstrates the CVs on $Ni_{50}Pd_{50}$/G at different scan rates in an 0.4 M ethanol-containing 1 M KOH solution. The relationship between both f and b-peak current density and $v^{1/2}$ is displayed (inset a). The current densities for EOR become bigger with an increasing scan rate. The linear relationship can be observed between current densities and $v^{1/2}$, which suggests the EOR on $Ni_{50}Pd_{50}$/G is a diffusion-controlled process.[51] Furthermore, the f-peak potential increases with increasing scan rate, and a straight line relationship can be observed between f-peak potentials and ln of scan rates (inset b), suggesting the EOR on $Ni_{50}Pd_{50}$/G is an irreversible electrode process.[51]

CA has used to evaluate the stability of the Ni_xPd_{100-x}/G BACs in 0.5 M EtOH-containing 1 M KOH with an applied potential of −0.4 V. As can be seen in Figure 8a, initial rapid current decreases could be attributed to the accumulation of strongly adsorbed intermediates onto the surface of reactive sites. Consequently, the relative current slowly decreased and reached a pseudo-steady state. The time-dependent comparison can be seen in the inset. The stability of Ni_xPd_{100-x}/G BACs were also investigated by the long-term CV sweep for 500 cycles (Figure S10), and the first CV cycle of all Ni_xPd_{100-x}/G BACs were compared with 20% Pt/C in Figure S11. The current density of forward peaks from CVs is shown in Figure 8b. From Figure 8, the stability of $Ni_{50}Pd_{50}$/G catalyst in terms of relative current is about 2.3, 2.7, and 3.5 times (from CA) and 2.4, 5.0, and 1.2 times (from CV) higher than Ni_0Pd_{100}/G, $Ni_{75}Pd_{25}$/G and $Ni_{25}Pd_{75}$/G, respectively. The indicates highly efficiency and poisoning tolerance on $Ni_{50}Pd_{50}$/G catalyst.[1,20,22] Both CV and chronoamperometric measurements conclude that $Ni_{50}Pd_{50}$/G has optimal EOR activity among Ni_xPd_{100-x}/G BACs.

CONCLUSION

In summary, a series of electrocatalyst, G-supported Ni_xPd_{100-x} BACs has been successfully synthesized via a simple chemical method and introduced to the EOR with superior catalytic activity. We were able to prepare the Pd and Ni alloy at low temperature with Ni being oxidized in the BACs through combined characterization techniques. In particular, the $Ni_{50}Pd_{50}$/G catalyst demonstrated higher peak current density, mass activity, and much negatively shifted onset potential (−0.8 V vs Ag/AgCl) in CV in EtOH 1 M KOH containing solution. Also, it showed long-term stability compared to the other BACs in both CA and CV. The $Ni_{50}Pd_{50}$/G catalyst had the lowest Tafel slope and highest level of alloy content that lead to a superior charge-transfer rate toward EOR. The overall dependence of both ethanol concentration and scan rate indicated that the $Ni_{50}Pd_{50}$/G is the more promising EOR catalyst. By comparing CVs and Tafel slopes, we concluded that the EOR on $Ni_{50}Pd_{50}$/G catalyst might mostly proceed by forming acetic acid. Also, we hope that this report will encourage other groups to prepare G-supported Ni−Pd materials for Pt-free catalytic applications including DEFCs.

EXPERIMENTAL SECTION

Synthesis of Graphene-Supported Ni_xPd_{100-x}. Graphene oxide (GO) was obtained from graphite powder via a modified Hummer's method.[10,11,29,36] Briefly, a mixture of 1 g of graphite powder and 6 g

dx.doi.org/10.1021/cs500103a | ACS Catal. 2014, 4, 1830−1837

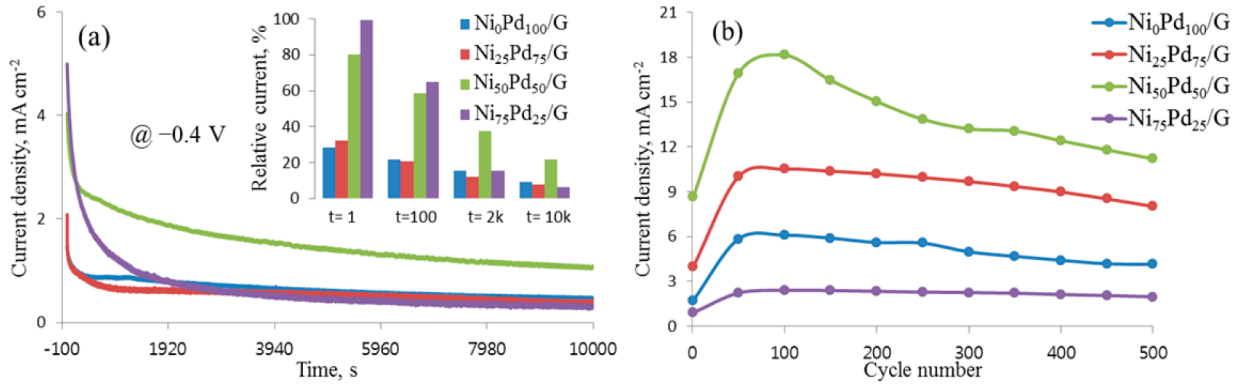

Figure 8. CA measurements and the plots of forward peak current density and cycle number (from Figure S10) of Ni_xPd_{100-x}/G BACs in 1 M KOH with 0.5 M EtOH solution. Inset: time-dependent current density comparison.

of $KMnO_4$ was added into a mixture of concentrated H_2SO_4 (120 mL) and H_3PO_4 (13 mL) in a round-bottom flux and was then stirred at 60 °C for 16 h. The reaction was poured onto 200 mL of ice followed by adding 2 mL of 30% H_2O_2 after cooling at RT. The yellow product was centrifuged at 4000 rpm, and the precipitate was then washed with 30% HCl, water (up to Cl^- was not removed), and EtOH. The remaining solid material was dispersed in ether and filtered. The final product, GO, was then vacuum-dried at 60 °C for 24 h.

The 0.01 M of K_2PdCl_4 and 0.01 M of $Ni(NO_3)_2{\cdot}6H_2O$ were mixed in a 20 mL vial (the atomic ratios of Ni and Pd were 0:100, 25:75, 50:50, and 75:25), followed by the addition of 5 mg of GO into the vial and prepare a yellow-brown homogeneous solution by ultrasonic agitation with no visible aggregated particles. This solution was kept under stirring at RT. Subsequently, 1 mL of 0.01 M ascorbic acid was added under continuous stirring for 30 min to prepare metal nanoparticles (NPs), and the color of the solution was changed into ash. Thereafter, 5 μL of 65% hydrazine (N_2H_4) was added under stirring for another 30 min, followed by continuous heating in an oven at 65 °C for overnight to produce a homogeneous black suspension. The finishing products (Ni_0Pd_{100}/G, $Ni_{25}Pd_{75}$/G, $Ni_{50}Pd_{50}$/G, or $Ni_{75}Pd_{25}$/G,) were collected through filtration and dried in a vacuum oven at 40 °C for 12 h.

Characterizations of Physical Parameters. All TEM images and EDS were obtained by TECNAI model FI-20 (FEI, Netherland). The FTIR measurements were performed on an FTIR spectroscope (PerkinElmer). XPS were gained using a MultiLab 2000 with a 14.9 keV Al K X-ray source. XRD spectra were carried out on a Rigaku D/max-2500, using filtered Cu Kα radiation.

Electrochemical Characterization. The suspension of Ni_0Pd_{100}/G, $Ni_{25}Pd_{75}$/G, $Ni_{50}Pd_{50}$/G, or $Ni_{75}Pd_{25}$/G in ethanol (1 mg mL^{-1}) was prepared separately by a 30 min sonication. A 5 μL portion of the Ni_0Pd_{100}/G, $Ni_{25}Pd_{75}$/G, $Ni_{50}Pd_{50}$/G, or $Ni_{75}Pd_{25}$/G suspension was then dropped onto the prepolished glassy carbon electrode (GCE, 0.3 cm in diameter) trailed by dropping 5 μL of Nafion solution as a binder (0.5 wt % in ethanol). The Pt/C suspension (20%) was prepared by dispersing 1 mg mL^{-1} of 20% Pt/C in ethanol in the presence of 5 μL of 5% Nafion solution in aliphatic alcohol and used 5 μL from the suspension onto GCE. All CVs and CA were taken using a three-electrode potentiostat [CHI 700C electrochemical workstation (U.S.A.)]. A Pt wire and Ag/AgCl electrodes were used as auxiliary electrode and reference electrode, respectively. All electrochemical experiments were performed in a high purity Ar purged (for at least 30 min) 1 M KOH solutions at RT.

■ ASSOCIATED CONTENT

Supporting Information

Supplemental TEM images, EDS spectra, XPS spectra, FTS spectra, and other additional data. This material is available free of charge via the Internet at http://pubs.acs.org.

■ AUTHOR INFORMATION

Corresponding Author

*E-mail: swjeon3380@naver.com. Fax: +82 62 530 3389. Tel.: +82 62 530 0064.

Notes

The authors declare no competing financial interest.

■ ACKNOWLEDGMENTS

This research has supported by the National Research Foundation of Korea (NRF) funded by the Ministry of Education,Science and Technology (2010-0007864).

■ REFERENCES

(1) Xu, H.; Ding, L.-X.; Liang, C.-L.; Tong, Y.-X.; Li, G.-R. *NPG Asia Mater.* **2013**, *5*, e69−e79.
(2) Lee, E.; Park, I.-S.; Manthiram, A. *J. Phys. Chem. C* **2010**, *114*, 10634−10640.
(3) Ahmed, M. S.; Jeon, S. *J. Power Sources* **2012**, *218*, 168−173.
(4) Lu, Y.; Jiang, Y.; Wu, H.; Chen, W. *J. Phys. Chem. C* **2013**, *117*, 2926−2938.
(5) Xia, B. Y.; Wu, H. B.; Wang, X.; Lou, X. W. *J. Am. Chem. Soc.* **2012**, *134*, 13934−13937.
(6) Zhang, L.; Li, N.; Gao, F.; Hou, L.; Xu, Z. *J. Am. Chem. Soc.* **2012**, *134*, 11326−11329.
(7) Yamauchi, Y.; Tonegawa, A.; Komatsu, M.; Wang, H.; Wang, L.; Nemoto, Y.; Suzuki, N.; Kuroda, K. *J. Am. Chem. Soc.* **2012**, *134*, 5100−5109.
(8) Dutta, A.; Datta, J. *J. Mater. Chem. A* **2014**, *2*, 3237−3250.
(9) Lim, B.; Kobayashi, H.; Yu, T.; Wang, J.; Kim, M. J.; Li, Z.-Y.; Rycenga, M.; Xia, Y. *J. Am. Chem. Soc.* **2010**, *132*, 2506−2507.
(10) Mondal, A.; Jana, N. R. *ACS Catal.* **2014**, *4*, 593−599.
(11) Wang, Y.; Zhao, Y.; Yin, J.; Liu, M.; Dong, Q.; Su, Y. *Int. J. Hydrogen Energy* **2014**, *39*, 1325−1335.
(12) Ma, L.; He, H.; Hsu, A.; Chena, R. *J. Power Sources* **2013**, *241*, 696−702.
(13) Ding, L.-X.; Wang, A.-L.; Ou, Y.-N.; Li, Q.; Guo, R.; Zhao, W.-X.; Tong, Y.-X.; Li, G.-R. *Sci. Rep.* **2013**, *3*, 1181−1188.
(14) Du, W.; Mackenzie, K. E.; Milano, D. F.; Deskins, N. A.; Su, D.; Teng, X. *ACS Catal.* **2012**, *2*, 287−297.
(15) Shen, S. Y.; Zhao, T. S.; Xu, J. B.; Li, Y. S. *J. Power Sources* **2010**, *195*, 1001−1006.
(16) Ahmed, M. S.; Kim, D.; Jeon, S. *Electrochim. Acta* **2013**, *92*, 168−175.
(17) Awasthi, R.; Singh, R. N. *Carbon* **2013**, *51*, 282−289.
(18) Zhang, Z. H.; Ge, J. J.; Ma, L.; Liao, J. H.; Lu, T. H.; Xing, W. *Fuel Cells* **2009**, *2*, 114−120.
(19) Zhang, M.; Yan, Z.; Xie, J. *Electrochim. Acta* **2012**, *77*, 237−243.
(20) Lee, K.; Kang, S. W.; Lee, S.-U.; Park, K.-H.; Lee, Y. W.; Han, S. W. O. *ACS Appl. Mater. Interfaces* **2012**, *4*, 4208−4214.

(21) Demirci, U. B. *J. Power Sources* **2007**, *173*, 11−18.
(22) Zhang, Z.; Xin, L.; Sun, K.; Li, W. *Int. J. Hydrogen Energy* **2011**, *36*, 12686−12697.
(23) Ding, K.; Yang, H.; Cao, Y.; Zheng, C.; Rapole, S. B.; Guo, Z. *Mater. Chem. Phys.* **2013**, *142*, 403−411.
(24) Ramulifho, T.; Ozoemena, K. I.; Modibedi, R. M.; Jafta, C. J.; Mathe, M. K. *Electrochim. Acta* **2012**, *59*, 310−320.
(25) Chun, C.; Yu, F.; Meng, H.; Chunying, W.; Guoqiang, S.; Lingyan, Z. *Appl. Catal. B: Environ.* **2013**, *142*−*143*, 553−560.
(26) Barakat, N. A. M.; Motlak, M.; Elzatahry, A. A.; Khalil, K. A.; Abdelghani, E. A. M. *Int. J. Hydrogen Energy* **2014**, *39*, 305−316.
(27) Singh, R. N.; Awasthi, R. *Catal. Sci. Technol.* **2011**, *1*, 778−783.
(28) Seo, M. H.; Choi, S. M.; Seo, J. K.; Noh, S. H.; Kim, W. B.; Han, B. *Appl. Catal. B: Environ.* **2013**, *129*, 163−171.
(29) Zhang, M.; Yan, Z.; Sun, Q.; Xie, J.; Jing, J. *New J. Chem.* **2012**, *36*, 2533−2540.
(30) Novoselov, K. S.; Geim, A. K.; Morozov, S. V.; Jiang, D.; Katsnelson, M. I.; Grigorieva, I. V.; Dubonos, S. V.; Firsov, A. A. *Nature* **2005**, *438*, 197−200.
(31) Geim, A. K.; MacDonald, A. H. *Phys. Today.* **2007**, *60*, 35−41.
(32) Balandin, A. A.; Ghosh, S.; Bao, W.; Calizo, I.; Teweldebrhan, D.; Miao, F.; Lau, C. N. *Nano Lett.* **2008**, *8*, 902−907.
(33) Lee, C.; Wei, X.; Kysar, J. W.; Hone, J. *Science* **2008**, *321*, 385−388.
(34) Stankovich, S.; Dikin, D. A.; Dommett, G. H. B.; Kohlhaas, K. M.; Zimney, E. J.; Stach, E. A.; Piner, R. D.; Nguyen, S. B. T.; Ruoff, R. S. *Nature* **2006**, *442*, 282−286.
(35) Guo, S.; Dong, S.; Wang, E. *ACS Nano* **2010**, *4*, 547−555.
(36) Marcano, D. C.; Kosynkin, D. V.; Berlin, J. M.; Sinitskii, A.; Sun, Z.; Slesarev, A.; Alemany, L. B.; Lu, W.; Tour, J. M. *ACS Nano* **2010**, *4*, 4806−4814.
(37) Zhang, H.; Jin, M.; Wang, J.; Kim, M. J.; Yang, D.; Xia, Y. *J. Am. Chem. Soc.* **2011**, *133*, 10422−10425.
(38) Niu, W.; Zhang, L.; Xu, G. *ACS Nano* **2010**, *4*, 1987−1996.
(39) Wang, Y.; Wang, X.; Li, C. M. *Appl. Catal. B: Environ.* **2010**, *99*, 229−234.
(40) Ahmed, M. S.; Han, H. S.; Jeon, S. *Carbon* **2013**, *61*, 164−172.
(41) Li, R.; Wei, Z.; Huang, T.; Yu, A. *Electrochim. Acta* **2011**, *56*, 6860−6865.
(42) Maiyalagan, T.; Scott, K. *J. Power Sources* **2010**, *195*, 5246−5251.
(43) Wang, Y.; Shi, F.-F.; Yang, Y.-Y.; Cai, W.-B. *J. Power Sources* **2013**, *243*, 369−373.
(44) Qin, Y. H.; Yang, H. H.; Zhang, X. S.; Li, P.; Zhou, X. G.; Niu, L.; Yuan, W. K. *Carbon* **2010**, *48*, 3323−3329.
(45) Feng, Y.-Y.; Liu, Z.-H.; Kong, W.-Q.; Yin, Q.-Y.; Du, L.-X. *Int. J. Hydrogen Energy* **2014**, *39*, 2497−2504.
(46) Lai, S. C. S.; Kleijn, S. E. F.; Ozturk, F. T. Z.; Vellinga, V. C. V. R.; Koning, J.; Rodriguez, P.; Koper, M. T. M. *Catal. Today* **2010**, *154*, 92−104.
(47) Zhou, Z.-Y.; Wang, Q.; Lin, J.-L.; Tian, N.; Sun, S.-G. *Electrochim. Acta* **2010**, *55*, 7995−7999.
(48) Chen, L. Y.; Chen, N.; Hou, Y.; Wang, Z. C.; Lv, S. H.; Fujita, T.; Jiang, J. H.; Hirata, A.; Chen, M. W. *ACS Catal.* **2013**, *3*, 1220−1230.
(49) Jiang, L.; Hsu, A.; Chu, D.; Chen, R. *Int. J. Hydrogen Energy* **2010**, *35*, 365−372.
(50) Lai, S. C. S.; Koper, M. T. M. *Phys. Chem. Chem. Phys.* **2009**, *11*, 10446−10456.
(51) Zhao, Y.; Yang, X.; Tian, J.; Wang, F.; Zhan, L. *Int. J. Hydrogen Energy* **2010**, *35*, 3249−3257.